# Late-type dwarf irregular galaxies in the Virgo cluster.

# I. Hα and red continuum data

Ana Heller and Elchanan Almoznino

The Wise Observatory and the School of Physics and Astronomy

Tel Aviv University, Tel Aviv 69978, Israel

and

Noah Brosch[1]

Space Telescope Science Institute

3700 San Martin Drive

Baltimore MD 21218, U.S.A.

---

[1]On sabbatical leave from the Wise Observatory and the School of Physics and Astronomy, Raymond and Beverly Sackler Faculty of Exact Sciences, Tel Aviv University, Tel Aviv 69978, Israel

## ABSTRACT

We present H$\alpha$ and red continuum observations for a sample of late-type low surface brightness (LSB) dwarf irregular galaxies, consisting of all the ImIV and V galaxies with m$_B$ $\leq$17.2 in the Virgo cluster, and compare them with similar data for a representative sample of high surface brightness (HSB) dwarf irregular galaxies, also in the Virgo cluster. Line fluxes and equivalent widths are listed for individual HII regions and total H$\alpha$ emission is measured for the entire galaxies. Although significant line emission originates in the HII regions we identified, it does not make up the entire H$\alpha$ output of all galaxies.

For those objects of the LSB sample with H$\alpha$ emission we find typical star formation rates (SFR) of 6.9 $10^{-3}$ M$_\odot$ yr$^{-1}$, to as high as 4.3 $10^{-2}$ M$_\odot$ yr$^{-1}$. This is, on average, one order of magnitude weaker than for HSB objects, although the SFR overlap. On average, $\sim$2 HII regions are detected per LSB galaxy, for a total of 38 HII regions among 17 galaxies with H$\alpha$ emission. The HII regions are smaller and fainter than in HSB galaxies in the same Virgo cluster environment, have H$\alpha$ line equivalent widths about 50% of those in HSBs, and cover similar fractions of the galaxies. When more than one HII region is present in a galaxy we observe a strong intensity difference between the brightest and the second brightest HII region. The line-emitting regions of LSB galaxies are preferentially located at the periphery of a galaxy, while in HSBs they tend to be central. The H$\alpha$ line strength of an HII region is correlated with the red continuum light underneath the region; this holds for both LSBs and HSBs.

We do not identify fundamental differences in the star formation properties of the LSB and HSB dwarf galaxies we studied and infer that

these galaxies must be similar, with the difference being the intensity of the present star-formation burst.

*Subject headings:*   galaxies: dwarf - galaxies: irregular - galaxies: stellar content - HII regions - Virgo cluster

## 1. Introduction

The surface brightness of a galaxy is primarily determined by the stellar luminosity function and by the projected density of stars and these depend on the past and ongoing star formation. Much of our current understanding of the star formation (SF) phenomena on all scales is biased by the high surface brightness (HSB) objects that define the classical Hubble sequence. However, irregular galaxies in general, and dwarfs in particular, offer unique tests of SF models since they lack the more complex SF-triggering mechanisms, such as prominent spiral arms with the associated density waves and differentially rotating disks.

Low surface brightness (LSB) galaxies are defined as objects with central blue surface brightnesses $\mu(B)_o > 23$ mag arcsec$^{-2}$. Recent studies of LSB spiral (Sc and later) galaxies (McGaugh *et al.* 1995; de Blok *et al.* 1995) indicate that these are slowly evolving systems. The indication of a slow evolution but not full quiescence is based on the blue colours, presence of HII regions, low metallicites, extended gas disks, and high M(HI)/L ratios. The relative isolation of these systems and the low density of their gas component may be the reasons for the small amplitude SF bursts, and therefore the low overall star formation rates (SFR).

The SF history of a quiescent galaxy with a suitable gas reservoir in a cluster environment may be influenced by external factors such as the temperature of the hot intra-cluster medium (ICM) and the galaxy's interaction with other cluster galaxies and with the intra-cluster medium. Therefore it is important to choose carefully the environment of a sample of galaxies studied to learn about star formation processes. Recent work on HSB dwarf galaxies (DGs) in the Virgo cluster (blue compact dwarf BCD or ImIII/BCD: Almoznino 1996; Almoznino & Brosch 1998, AB98) points to a possible evolutionary connection between their rather blue underlying stellar component and LSB DGs. We approach these questions here by analyzing optical narrow and broad-band

CCD observations of fainter luminosity objects (ImIV-V) in the same environment, the Virgo cluster (VC). Both samples (HSB and LSB) comprise altogether 47 late-type irregular galaxies.

In this paper we concentrate on the morphology of HII regions in our sample of LSB galaxies, and on the star formation rates (SFR) derived from galaxy-wide H$\alpha$ fluxes as well as from individual HII regions for the objects in the LSB sample. We compare these with similar observables from the HSB sample of dwarf galaxies presented in AB98. The H$\alpha$ radiation is directly coupled to the radiation shorter than $\lambda < 912$Å and originates from OB stars of lifetime $\simeq 5 \times 10^6$ years, indicating on-going massive star formation, while optical broad-band colours provide information on older stellar populations. The surface photometry of the galaxies in our sample through UBVRI filters, with calibrated fluxes, radial surface brightness, contour colour maps and profiles, central surface brightness, and scale lengths shall be presented in forthcoming papers along with a full analysis of the entire data set.

The plan of the paper is as follows: we first describe the sample in section 2, then the observations we performed and their reduction in section 3. The results are discussed in section 4 and our findings are summarized in section 5.

## 2. The sample

The selection of LSB galaxies is based primarily on the morphological classification of DGs in the VC (Binggeli *et al.* 1985, VCC). We selected galaxies listed in VCC as Magellanic Irregulars of sub-types ImIV or ImV with $m_B \leq 17.2$ and members in the VC. The faintest ImV galaxies listed in VCC have $m_B = 17.5$, thus our selection is safely distant from the limit of the VCC cutoff. All our galaxies have single dish HI measurements with detected non-zero total flux from the Arecibo survey of VCC

late-type dwarf galaxies of Hoffman *et al.* (1987). We imposed a recession velocity limit of 3,000 km sec$^{-1}$ to prevent the inclusion of background objects.

We adopt here a uniform sample distance of 18 Mpc for which 1"=87 pc. This assumption is justified as being the representative distance to galaxies within the Virgo cluster (*e.g.,* Fouqué *et al.* 1990). Other distance estimates are in the same range: 16.0±1.5 Mpc (van den Bergh 1996), 17.2-17.4 Mpc (Gonzalez & Faber 1997), 20.7±2.4 Mpc (Federspiel *et al.* 1998). Note though that the VC has significant depth, thus the assumption that all galaxies are at the same distance is probably true only at the 10% level. As most of our conclusions are drawn from ratios of quantities measured in the same galaxy, an even larger error in the distance will have no effect. The fluxes and flux densities would, however, change.

The sample, as defined here, is complete and is representative of LSB dwarf galaxies, though not of the lowest surface brightness ones. The reason is that galaxies with even fainter surface brightness exist, in the same neighborhood, and to study them as done here for ImIV-V objects is difficult and requires extensive observing time at major telescopes.

The 27 galaxies in the LSB sample are listed in Table 1. We identify them by their number in the VCC and list their total blue magnitude (which is an eye estimate from VCC), the total red magnitude (measured here, as explained below, and presented with a measurement error), the measured semi-major axis $a$ of the optical image in arcsec and ellipticity $e = 1 - \frac{b}{a}$ derived from an ellipse fit to the 25 mag arcsec$^{-2}$ isophote, and the H$\alpha$ results. The latter are given as total flux, total equivalent width, and fractional coverage of a galaxy by HII regions. The projected distribution of the objects in the VC is shown in Figure 1, where each object is marked as a circle with a diameter proportional to its apparent magnitude.

We added in the figure the galaxies from the HSB sample (filled circles, N=16)

discussed in AB98, and indicated the various sub-clusterings in the VC identified in Hoffman *et al.* (1989). The HSB sample shall be compared at various points of this paper with the LSB objects and some information, appearing already in AB98, shall be repeated here. This HSB comparison sample is composed of irregular galaxies, and the objects were selected to belong to the morphological class "blue compact dwarf" (BCD).

## 3. Observations and Reduction

Most LSB images analyzed here were obtained with the Wise Observatory (WO) 1.0-m telescope using a TEK 1024×1024 pixel thinned and back-illuminated CCD. This chip has a very low read-out noise ($6.5$ e$^{-1}$) and its quantum efficiency in the regions of interest is high ($\sim$80% at 6500Å). The plate scale for the WO images is 0".7 pixel$^{-1}$. One galaxy studied here was observed by EA in 1992 at the WO using an RCA CCD with 0".9 pixels (see AB98). A few exposures were obtained by NB at the $f/4$ Prime Focus of the Russian Academy of Sciences' Special Astrophysical Observatory 6.0-m (BTA) telescope. The CCD used for those observations was a 512×512 array, with a projected pixel size of 0.154"×0.205". The readout noise of the device used on the BTA was 30 e$^{-}$ and the conversion from DNs was 13.8 e$^{-}$=1 DN. The BTA images were binned off-line $4 \times 3$ pixels, which gives 0".615 square pixels, comparable to the plate scale of the WO images.

The image sets analyzed here consist of line and continuum images for each galaxy obtained from 1995 to 1997. We collected three 1800 sec (WO), or two 600 sec (BTA), exposures through the line filter and an equal number of continuum exposures per object. The line filters were chosen to match, as far as possible, the rest frame H$\alpha$ emission of each galaxy and are described in AB98. We used a $\sim$53Å filter centered on 6700Å for measuring the continuum contribution. The reduction was done with IRAF and the flux calibration used observations of HZ44, which was measured several times each

night through different air masses with the same filters as used for the galaxies. Note that though this standard star shows H$\alpha$ and HeI absorptions, these do not affect the calibration because the filters used here are redshifted with respect to these features in the standard.

The images were debiased, flat fielded with twilight frames, and cosmic rays and hot pixels were removed with standard IRAF tasks. The images through the same filter were co-added after being registered by cross-correlation. The sky background was subtracted as a tilted plane fitted to the final combined image in each band, after the galaxy and the bright stars were masked off. The standard deviation of the fitted plane from the actual background light distribution was used to estimate the noise introduced by sky subtraction.

The images were calibrated in flux using the observations of HZ44 and were convolved with a 2"-4" FWHM gaussian, according to the seeing. We then performed aperture photometry on stars in the field, normalizing the results of the line and continuum bands. In this way we also corrected for any relative change of continuum sloping in the two bands. The scaling between the on-line to off-band images was applied to the full resolution images and the net fluxed H$\alpha$ images were derived by subtracting off-line from on-line fluxed images. As expected, the stars vanished from the net image, with the exception of cases where imperfect PSF matching caused small distortion near very bright stars. This method is very similar to that used successfully by *e.g.,* Hodge (1969), Hunter & Gallagher (1986), and recently Gavazzi *et al.* (1998).

The photometry, and the derivation of line and continuum fluxes, are based on measurements of the HZ 44 spectrophotometric standard and flux scaling from it to the galaxy, after correcting for differential extinction. We estimate the photometric accuracy from the extinction coefficients obtained for the ON and OFF bands; these are both 0.19±0.12 and are consistent with the long-term average of the R-band

extinction coefficient at the Wise Observatory (0.21; Brosch 1992). As the typical airmass differences between observations of the standard and of the target galaxies were always ≤0.3, this indicates that the error which could be attributed to extinction is at most ∼0.06 mag.

The off-line continuum images were smoothed to a 1" resolution and iso-intensity contours were traced around each galaxy. Polygonal apertures were defined by the contour level of 25 mag arcsec$^{-2}$ isophote. Generally, this isophote level corresponded to a $S/N = 1$ per pixel in the final images for all galaxies. The total H$\alpha$ flux from the galaxies was obtained by measuring within the polygonal aperture the averaged $f_\lambda$ in the net emission images and multiplying the results by the FWHM of the H$\alpha$ line filter. We did not compensate for the contribution of [NII] lines to the derived H$\alpha$ fluxes, as the ratio $\frac{[NII]}{H\alpha}$ in dwarf irregular galaxies is expected to be small due to their generally low metal abundances (Gallagher & Hunter 1989, Skillman *et al.* 1989).

The red continuum emission from each galaxy, f(OFF), in flux density units, was also measured within the same polygonal aperture. The total flux was transformed into monochromatic magnitudes at ∼6700Å (m$_{67}$), which are listed in Table 1. The ratio between the net H$\alpha$ emission and the red continuum flux measured from the off-line image is the emission line equivalent width (EW). Although it is not yet clear which stellar population is responsible for this red emission, *i.e.,* whether it is produced by the stars formed in the present SF event or by a pre-existing stellar population, we list these EW values along with the line fluxes in Table 1. The "monochromatic" magnitude at $\lambda \simeq 6700$Å is not equivalent to the R-band magnitude; a transformation of the flux density for a zeroth magnitude star in Bessel (1979) for the R$_c$ band into the monochromatic magnitude system yields m$_{67} \simeq 0.44$. Therefore, the use of this system introduces some zero-point shifts. The errors, in both the line and continuum measurements, are derived from the rms combination of the errors of the polygon

photometry of the galaxy and the calibration of the spectrophotometric standard star.

We could not measure the dimensions of the red continuum image for VCC 381 because of its exceeding faintness. The numbers quoted in parentheses in Table 1 are from NED. In the case of VCC 2034 a star is projected against the galaxy; we could not subtract accurately its contribution to enable a reliable determination of $m_{67}$. Similar data for the HSB sample are presented in Table 2. This is done here only for the purpose of completeness and comparison; the full data set relevant for the HSB galaxies is part of the AB98 paper and is discussed there. We note that the entire sample consists of "dwarf" galaxies, as they all have $M_B > -18$. The two samples studied here are thus representative of the late-type dwarf irregular kind, and they come in two "flavors" of high or low surface brightness.

Table 2 lists the $m_B$ and $m_R$ magnitudes for the HSB galaxies; these are the values actually measured through the broad-band B and R filters (where the latter contains $H\alpha$ and [NII] contributions). The level of line contamination of the R magnitude can be estimated from the equivalent width of $H\alpha$. In contrast, Table 1 lists the $m_B$ estimated in the VCC for the LSBs, and gives as $m_{67}$ the measured monochromatic magnitude of the continuum, which is free of line contamination.

Table 3 presents the statistics of detections of HII regions in our two samples (HSB from AB98 and LSB discussed here) and the last column of Tables 1 & 2 lists the on-going global average SFR of each galaxy, derived from the relation of Kennicutt $et$ $al.$ (1994) scaled to the 18 Mpc adopted distance of the VC: SFR=2.93 $10^{11}$ F($H\alpha$), where F($H\alpha$) is the total line flux in erg s$^{-1}$ cm$^{-2}$ and the SFR is in $M_\odot$ yr$^{-1}$.

Finally, we also measured the fluxes from the individual HII regions which were identified in the $H\alpha$ images by integrating the net flux collected within a circular aperture around each HII region. The size of this aperture was determined by first visually inspecting the net line image using the IMEXAM task from IRAF, followed by PHOT

with a number of apertures. This aperture size taken here to represent the size of the HII region is that where an increase in size did not add more flux. The individual HII region fluxes are listed in Table 4. We also list there the SFR derived for each HII region, as well as the flux in the red continuum underneath it, along with the line EW and the individual SFR derived for the specific HII region, as explained above. The errors listed for the HII regions are only photometric. For completeness, we list in Table 5 similar parameters for the HII regions in the HSB sample. The HII regions are identified by the name of the galaxy in column 1, and by the label given to the HII region in the specific figure in column 2. The HSB data equivalent to these presented in Table 1 for the LSB galaxies have been published in AB98.

## 4. Results

Figures 2 through 7 present mosaic images of the LSB galaxies observed at the WO. We show three to five galaxies per figure in horizontal rows. Each row contains the image through the line filter at the left, the image through the continuum filter in the middle, and the net Hα image at the right. Each top-right image on a page of LSBs has a scale mark near its top-right corner; the mark is 10 arcsec long (=870 pc at the adopted distance of the VC) and indicates the scale of all the images on the page. Fig. 8 shows the two galaxies observed at the BTA and the single galaxy from the LSB sample observed at WO by EA with a different CCD. Figs. 9, 10, and 11 show the BCD galaxies from AB98 in the same format as used here for the LSB objects, for comparison and completeness. These images have not been presented elsewhere. Figs. 8 to 11 have individual 10 arcsec bars for each object. For each galaxy we marked and labelled the individual HII regions we recognized in the net Hα image.

The underlying LSB galaxies, measured on the red continuum images, have an average major axis diameter of 58"≈5 kpc. For comparison, the average major axis of

the HSB sample is 40"≈3.5 kpc.The semi-major axes of the LSB galaxies are listed in Table 1, along with the ellipticity parameter $e$. These were derived from the fit of an ellipse to the red continuum light at the 25 mag arcsec$^{-2}$ isophote. We also list there $f$, the fractional coverage of a galaxy by HII regions. This is obtained by dividing the sum of all aperture areas with which we measured the individual HII regions by the area of the "continuum" galaxy, defined by the measuring polygon described above.

We identified 38 HII regions, single or in complexes, in 17 galaxies of the LSB sample. Due to the limiting spatial resolution of this study (∼300 pc at the VC), and the limiting surface brightness, we were not able in some cases to separate individual small HII regions from their nearest neighbours, nor to detect the faintest HII regions. Therefore our survey was sensitive to HII "complexes" of typical sizes larger than the 300 pc resolution limit or to giant HII regions. About half of the galaxies with H$\alpha$ emission have a single HII region and the rest have two or more regions. In two cases (VCC 17 and VCC 826), and possibly in VCC 328 as well, the HII regions seem to be arranged on the circumference of a circle or an ellipse. In VCC 17 it seems that the center of this distribution shows an HII region as well; in VCC 826 the center seems empty. We emphasize that the localization of the HII regions on the circumference of an ellipse is a subjective result; we have not attempted to fit such an ellipse to the distribution of the HII regions, and indeed such a fit may not succeed in a number of cases because of the strong intensity of one HII region compared with others in the same galaxy.

In contrast with the LSB galaxies, the HSB objects show, in most cases, strong H$\alpha$ emission originating from a single HII region. The line-emitting region is similar in size to the entire galaxy. The global H$\alpha$ emission, in terms of the line equivalent widths, shows that the LSB sample has more low EW values and the global line emission hardly reaches 100Å, whereas in the HSB sample ∼1/3 of the HII regions reach or exceed this value. The entire issue of the morphology of star formation in irregular galaxies is

discussed in another paper (Brosch *et al.* 1998a).

The data in Table 3 indicates that the difference between HSB and LSB galaxies is more pronounced when considering HII regions than for entire galaxies. The difference in median SFRs for individual SF regions is more than one order of magnitude; the HSBs have much more intense SF than LSBs. We compare in Fig. 12 the SFRs found for individual HII regions in the sample of HSB galaxies from AB98 and in the sample of LSBs studied here. We included all the listed H$\alpha$ values, not only those higher than the 1.5$\sigma$ level. In general, HII regions in HSB galaxies show more intense SFR, by 0.5 dex on average relative to HII regions in LSBs. However, there are HII regions in objects classified as Blue Compact Galaxies which show SFR levels as low as those in some LSBs. This is not exceptional, as in both groups of galaxies there are cases where no H$\alpha$ emission is observed. In addition, we note that not only is the H$\alpha$ emission from HII regions in HSBs more intense than in LSBs, but also the line equivalent width is higher (median H$\alpha$ EW in LSBs is 47Å *vs.* 80Å in HSBs).

## 5. Discussion

The properties of star formation, derived from the surface brightness of H$\alpha$, have been discussed by Brosch *et al.* (1998b). Briefly, in dwarf irregulars the average H$\alpha$ surface brightness correlates reasonably well with the mean blue surface brightness ($\sigma_B$). If the SF process is regulated on a local scale, the correlation should be tighter if we consider only the HII regions, and not the entire galaxies. We therefore test here the correlation of H$\alpha$ emission against the red continuum surface brightness for individual HII regions. This is preferred to $\sigma_B$, because it is determined here independently as part of the derivation of the H$\alpha$ brightness. We show in Figure 13 the correlation between the H$\alpha$ flux of an HII region and the red continuum emission underlying the region, as measured on the off-line image with the same aperture as used for the H$\alpha$ measurement

of the LSB sample (stars). Although a trend for more intense line emission when the red continuum is more intense seems to be present, it is by no means tight. A formal linear regression indicates a correlation coefficient of 0.62 (F=23)[2]. A similar regression for the fewer HII regions in BCDs (filled squares) shows a tighter relation (correlation coefficient 0.82, F=32). Both correlations are significant and indicate the regulation of the SF activity by the local population of stars. In particular, note that the two samples "line-up" nicely on the plot, indicating that the connection between H$\alpha$ line strength and underlying line continuum brightness transcends the morphological type of a galaxy.

An inspection of Table 4 and of Figs. 2 to 7 indicates that in most cases of multiple HII regions in LSB galaxies one is much brighter than the others. This indicates that either the star formation does not occur simultaneously within the galaxy, or that if it does, not all star-forming sites reach the same strength of star formation at the same time. The fraction of objects with more than one HII region among the HSB sample is much smaller, but the cases of VCC 1374, and to a lesser degree of VCC 1725 and VCC 1791, are similar. We can quantify this difference between HII regions in the same galaxy with the data in Table 4: the H$\alpha$ flux ratio between the brightest HII region and the second brightest is $\sim$3 (median 2.3) and the similar ratio of equivalent widths is $\sim$2.

Not all H$\alpha$ emission from an irregular galaxy originates in the bright HII regions. We compared the summed H$\alpha$ line flux from the HII regions of one galaxy listed in Tables 3 and 4 with the integrated line emission from the same galaxy (Tables 1 and 2) and found that a significant fraction of the H$\alpha$ flux is not recovered. In particular, for VCC 17, VCC 260, and VCC 530 the HII regions we identified produced less than 70% of

---

[2]F is the ratio between the mean square deviation due to the regression and the mean square deviation due to the residual variation. For a linear regression, which is the present situation, F=t$^2$ and this is the equivalent of a t-test. For more details see Draper & Smith 1981.

the total galaxy line output (but more than 50%). In a number of objects where we did not detect individual HII regions we nevertheless measured a significant H$\alpha$ flux (VCC 329, VCC 1816, and VCC 2034; all detected in the line at the $3\sigma$ level and all from the LSB sample). However, in eight objects it seems that virtually the entire H$\alpha$ output originates in the individual HII regions. It is clear that the detection of an HII region is a combination of compactness, signal strength, and contrast against the background of this region.

We find that the fractional coverage of a galaxy by HII regions (the ratio between the summed areas of the apertures with which we measured the HII regions and the total area of a galaxy on the red continuum image) is amazingly similar between LSB and HSB objects and in both cases it peaks near 50%, as Figure 14 shows. The average value of $f$ in HSB objects is $\sim 2\times$ larger than in LSB objects, but the median values are similar: 38% for the LSBs and 43% for the HSBs. As is often the case with small samples, the median values are more representative of the "typical" behavior than the means, which are driven by outlier values. However, it seems that the HSB galaxies lack the faint HII regions which are detected in the LSB sample.

The location of HII regions within the red continuum envelope, which presumably traces the distribution of old stars or of red supergiants, shows an interesting trend: in the large majority of cases where a galaxy has HII regions, these appear preferentially at the periphery of the red envelope. Only two cases of possibly central ("nuclear") HII regions have been identified: VCC 963 and VCC 1455. In three other cases the HII regions were indiscriminately distributed over the red surface of the galaxies, with no special preference to either center or periphery.

The trend of SF activity to be relegated to the periphery of irregular galaxies is discussed in more detail in Brosch $et\ al.$ (1998a) and could, in principle, indicate a coupling between the interstellar matter in a galaxy and the gas in the surroundings of

the galaxy. This has been suggested as a possible explanation of lop-sided SF activity in the LMC (de Boer *et al.* 1998). In this case, the SF activity could be triggered by some sort of shear or pressure which compresses the ISM in the galaxy and starts making stars, which then move away from the location of formation and age. The difference between the brightest HII region and the other HII regions of the same LSB galaxy could, in this case, be the result of aging. The prediction from this scenario is that as an HII region gets older its total line emission flux decreases while the underlying red continuum emission increases (because of the contribution from the aging stars on top of that from any previous stellar populations), thus its line EW decreases sharply. We can test this using the data presented here.

We calculated the "contrast" in line emission and in underlying continuum emission for those objects which show multiple HII regions. Specifically, we calculated the ratio between the H$\alpha$ fluxes of the most intense HII region and the least intense one in a galaxy, and plotted this in Figure 15 against the ratio of the red continua flux densities of the same two HII regions. The distribution of points shows that the stronger H$\alpha$ emission is related to the more intense red continuum, an opposite trend (to first order) than expected from an assumption of SF activation by interaction with external gas. The correlation is low (0.51, F=4) but indicative and the trend, being opposite to what was expected, allows us to reject the hypothesis. On the other hand, a regulation of the SF by the local star density would make a plausible possibility and would fit well with our finding that the SFR per unit solid angle correlates with the blue surface brightness (Brosch *et al.* 1998b).

## 6. Conclusions

We studied a sample of very low surface brightness irregular galaxies in the Virgo cluster and found that the majority show indications of current star formation. We

summarize our findings as follows:

1. The LSB galaxies have a modest total SFR, typically of $\sim 7 \ 10^{-3}$ $M_\odot$ $yr^{-1}$, while HSB galaxies have a typical SFR of $\sim 6 \ 10^{-2}$ $M_\odot$ $yr^{-1}$.

2. The typical global H$\alpha$ equivalent width of LSBs is $\sim 2\times$ lower than in BCDs.

3. The HII regions of BCD galaxies tend to be centered on the red continuum images of the galaxies.

4. LSB galaxies in which we detected multiple HII regions have one very bright region with others much fainter, mostly located at the edges of galaxies.

5. On average, there are $\sim 2$ HII regions per LSB galaxy. They are smaller and fainter than those found in the BCDs of the Virgo Cluster.

6. The fractional coverage of a galaxy by HII regions is similar in LSBs and in BCDs, and so is the equivalent width of the line produced by individual HII regions.

7. The HII regions we detected produce more than half of the total H$\alpha$ line emission of an LSB galaxy, and in many cases the entire galaxy line emission.

8. The strength of the H$\alpha$ emission from an HII region is correlated with the intensity of the red continuum underneath the HII region in both (HSB and LSB) samples.

Our findings do not indicate that there is a fundamental and basic difference between LSB and HSB irregular galaxies in their star-forming properties as reflected in their H$\alpha$ emission and its relation to the underlying red continuum light, but support the possibility that these two types of objects represent similar phenomena, which differ only in the intensity of the star formation process.

## Acknowledgments

## References

Almoznino, E. 1996, PhD thesis, Tel Aviv University.

Almoznino, E. & Brosch, N. 1998, MNRAS, in press (AB98).

Bessel, M.S. 1979, PASP, 91, 589.

Binggeli, B., Sandage, A. & Tammann, G.A. 1985, AJ, 90, 1681 (VCC).

Brosch, N. 1992, QJRAS, 33, 27.

Brosch, N., Heller, A. & Almoznino, E. 1998a, MNRAS, in press.

Brosch, N., Heller, A. & Almoznino, E. 1998b, ApJ, 504, in press.

de Blok W.J.G., van der Hulst J.M. & Bothun, G.D. 1995, MNRAS, 274, 235.

de Boer, K.S., Braun, J.M., Vallenari, A. & Mebold, U. 1998, A&A, 329, L49.

Draper, N.R. & Smith, H. 1981, *Applied Regression Analysis*, New York: Wiley, p. 32.

Federspiel, M., Tammann, G.A. & Sandage, A. 1998, ApJ, 495, 115.

Fouqué, P., Bottinelli, L., Gouguenheim, L. & Paturel, G. 1990, ApJ, 349, 1.

Gallagher, J.S. & Hunter, D.A. 1989, AJ, 98, 806.

Gavazzi, G., Catinella, B., Carrasco, L., Boselli, A. & Contursi, A. 1998, AJ, 115, 1745.

Gonzalez, A.H. & Faber, S.M. 1997, ApJ, 485, 80.

Hodge, P. 1969, ApJ, 156, 847.

Hoffman, G.L., Helou, G., Salpeter, E.E., Glosson, J. & Sandage, A. 1987, ApJS, 63, 247.

Hoffman, G.L., Williams, H.L., Salpeter, E.E., Sandage, A., Binggeli, B. 1989, ApJS, 71, 701.

Hoffman, G.L., Helou, G., Salpeter, E.E., Lewis, B. M. 1989, ApJ, 339, 812.

Hunter, D.A. & Gallagher, J.S. 1986, PASP, 98, 5.

Kennicutt, R.C., Tamblyn, P. & Congdon, C.W. 1994, ApJ, 435, 22.

Marlowe, A.T., Meurer, G.R. & Heckman, T.M 1997, ApJS, 112, 285.

McGaugh, S.S., Bothun G.D. & Schombert J.M. 1995a, AJ, 110, 573.

McGaugh, S.S., Schombert, J.M. & Bothun G.D. 1995b, AJ, 109, 2019.

Skillman, E.D., Kennicutt, R.C. & Hodge, P.W. 1989, ApJ, 347, 883.

van den Bergh, S. 1996, PASP, 108, 1091.

Table 1.   LSB dwarf sample

| VCC | $m_B$ | $m_{67}$ | a | e | f | F(H$\alpha$) | EW(H$\alpha$) | log(SFR) |
|-----|-------|----------|---|---|---|--------------|---------------|----------|
| 17 | 15.20 | 15.95±0.06 | 46 | 5 | 24 | 14.78±0.68 | 105±15 | −1.36 |
| 168 | 17.10 | 16.03±0.07 | 22 | 3 | 0 | -2.94±1.20 | 0 | 0 |
| 169 | 16.50 | 16.78±0.10 | 20 | 3 | 6 | 0.44±0.29 | 7±5 | −3.49 |
| 217 | 15.50 | 16.60±0.06 | 56 | 7 | 38 | 2.26±0.15 | 29±3 | −2.17 |
| 260 | 15.70 | 16.49±0.06 | 27 | 2 | 9 | 0.28±0.11 | 3±1 | −3.09 |
| 328 | 16.90 | 16.24±0.06 | 33 | 6 | 45 | 2.12±0.10 | 20±1 | −2.21 |
| 329 | 16.80 | 18.00±0.10 | 8 | 0 | 0 | 0.37±0.12 | 17±7 | −2.96 |
| 350 | 17.05 | 17.97±0.07 | 19 | 7 | 30 | 0.34±0.04 | 16±2 | −3.00 |
| 367 | 17.20 | 16.84±0.06 | 22 | 2 | 0 | -0.03±0.66 | 0 | 0 |
| 381 | 16.50 | 16.42±0.27 | (24) | (7) | 0 | 0.16±0.43 | 2±5 | −3.33 |
| 477 | 16.96 | 16.96±0.15 | 27 | 0 | 6 | 0.33±0.14 | 7±3 | −2.96 |
| 530 | 15.80 | 15.43±0.12 | 41 | 2 | 6 | 0.77±0.31 | 3±1 | −2.65 |
| 565 | 15.70 | 16.46±0.08 | 19 | 2 | 0 | 1.67±0.80 | 19±13 | −2.31 |
| 584 | 15.80 | 15.92±0.05 | 28 | 1 | 0 | 0.08±0.50 | 1±4 | −3.63 |
| 826 | 15.00 | 15.23±0.05 | 59 | 4 | 22 | 2.59±0.29 | 9±2 | −2.12 |
| 963 | 17.20 | 17.00±0.05 | 37 | 1 | 85 | 1.73±0.16 | 28±5 | −2.30 |
| 1455 | 16.80 | 16.29±0.07 | 23 | 4 | 75 | 1.70±0.13 | 17±2 | −2.30 |
| 1465 | 15.00 | 15.88±0.07 | 25 | 4 | 49 | 4.39±0.20 | 29±2 | −1.89 |
| 1468 | 15.00 | 15.87±0.09 | 28 | 4 | 25 | 3.50±0.31 | 23±3 | −1.99 |
| 1585 | 15.45 | 14.85±0.10 | 41 | 5 | 44 | 8.22±0.76 | 21±3 | −1.62 |
| 1753 | 16.81 | 18.04±0.06 | 16 | 2 | 81 | 0.68±0.05 | 32±4 | −2.70 |
| 1784 | 15.84 | 16.10±0.10 | 26 | 6 | 0 | 0.23±0.21 | 2±2 | −3.17 |
| 1816 | 16.20 | 16.16±0.15 | 28 | 6 | 0 | 1.87±0.60 | 16±7 | −2.26 |
| 1822 | 15.60 | 15.97±0.22 | 36 | 6 | 0 | -0.09±0.30 | 0 | 0 |
| 1952 | 16.00 | 16.63±0.10 | 22 | 5 | 45 | 2.39±0.70 | 32±16 | −2.15 |

Table 1—Continued

| VCC | $m_B$ | $m_{67}$ | a | e | f | F(H$\alpha$) | EW(H$\alpha$) | log(SFR) |
|------|-------|-------------|----|---|----|-----------|---------|--------|
| 1992 | 15.50 | 15.32±0.11 | 26 | 2 | 34 | 6.12±0.40 | 24±3 | −1.75 |
| 2034 | 15.82 | INDEF | 26 | - | 0 | 1.54±0.50 | 2±1 | −2.35 |

Note. — The total blue magnitude is the estimate from the VCC and e $m_{67}$ is the monochromatic magnitude of the continuum near 6700Å . The blue magnitudes of VCC 1585, 1753, and 1784 are a private communication from Bruno Binggeli and are different from the values listed in the VCC. The semi-major axis a is in arcsec and is derived from an ellipse fitting to the 25 mag arcsec$^{-2}$ isophote. The H$\alpha$ flux is in units of $10^{-14}$ erg cm$^{-2}$ s$^{-1}$. The ellipticity values are given as 10×e and are rounded off to single digits. The covering factor f is given in percent of the galaxy area in red continuum light. The SFR is in M$_\odot$ yr$^{-1}$ and is obtained by assuming a uniform distance of 18 Mpc to all galaxies.

Table 2.   HSB dwarf sample

| VCC | $m_B$ | $m_R$ | a | e | f | F(H$\alpha$) | EW(H$\alpha$) | log(SFR) |
|---|---|---|---|---|---|---|---|---|
| 10 | 16.20±0.09 | 14.88±0.10 | 24 | 5 | 98 | 9.30±1.90 | 31±7 | −1.56 |
| 22 | 16.83±0.03 | 15.82±0.05 | 5 | 2 | 0 | 0.5±2.0 | 0 | 0 |
| 24 | 16.12±0.03 | 14.89±0.07 | 22 | 3 | 0 | 1.50±4.90 | 0 | 0 |
| 144 | 15.29±0.03 | 14.61±0.03 | 13 | 3 | 100 | 70.5±7.6 | 235±25 | −0.68 |
| 172 | 15.38±0.03 | 14.53±0.03 | 27 | 6 | 0 | 0.37±0.60 | 1±2 | 0 |
| 324 | 14.58±0.03 | 13.62±0.02 | 29 | 2 | 74 | 63.1±4.3 | 210±14 | −0.73 |
| 410 | 17.76±0.04 | 16.89±0.04 | 9 | 2 | 100 | 0.50±0.05 | 1.7±0.2 | −2.83 |
| 459 | 15.29±0.04 | 14.40±0.07 | 22 | 2 | 38 | 29.7±3.3 | 99±11 | −1.06 |
| 513 | 15.84±0.03 | 14.56±0.02 | 13 | 2 | 52 | 21.7±2.0 | 72±7 | −1.20 |
| 562 | 16.59±0.03 | 15.86±0.05 | 11 | 3 | 48 | 13.4±0.9 | 45±3 | −1.41 |
| 985 | 16.62±0.04 | 15.61±0.07 | 13 | 5 | 23 | 3.1±1.8 | 10±6 | −2.04 |
| 1179 | 15.98±0.05 | 15.06±0.04 | 18 | 5 | 36 | 6.0±2.4 | 20±8 | −1.75 |
| 1374 | 15.00±0.02 | 14.19±0.02 | 32 | 6 | 59 | 29.7±1.3 | 99±4 | −1.06 |
| 1725 | 15.18±0.04 | 14.48±0.03 | 27 | 6 | 30 | 24.2±2.9 | 81±10 | −1.14 |
| 1791 | 14.85±0.04 | 14.09±0.03 | 36 | 7 | 29 | 40.3±1.9 | 134±6 | −0.93 |
| 2033 | 15.61±0.04 | 14.54±0.03 | 8 | 1 | 0 | 2.1±1.5 | 7±5 | −2.21 |

Note. — The total blue magnitude is the estimate from the VCC. The semi-major axis a is in arcsec and is derived from an ellipse fitting to the 25 mag arcsec$^{-2}$ isophote. The H$\alpha$ flux is in units of $10^{-14}$ erg cm$^{-2}$ s$^{-1}$. The ellipticity values are given as 10×e and are rounded off to single digits. The covering factor f is given in percent of the galaxy area in red continuum light. The SFR is in M$_\odot$ yr$^{-1}$ and is obtained by assuming a uniform distance of 18 Mpc to all galaxies.

Table 3.   HII region statistics in LSB and HSB samples

| Parameter | BCD | LSB |
|---|---|---|
| HII regions present | 12/16 (75%) [8/12 (67%) pure BCD] | 17/27 (63%) |
| Single HII region | 9/12 (75%) | 7/17 (42%) |
| Multiple HII regions | 3/12 (25%) | 10/17 (49%) |
| Covering factor of "continuum" galaxy | 67% (pure BCD) 57% (all galaxies) | 37% |

Note. — The covering factor listed in the last row is obtained by dividing the summed area of all HII regions by the area of the galaxy, as defined by the 25 mag arcsec$^{-2}$ isophote on the red continuum image.

Table 4.  Properties of individual HII regions in LSB galaxies

| Galaxy (VCC) | HII region ID | F(H$\alpha$) | f(OFF) | EW(H$\alpha$) | log(SFR) |
|---|---|---|---|---|---|
| 17 | a | 6.92±0.15 | 15±1.4 | 461 | −1.70 |
| 17 | b | 0.46±0.04 | 6.0±0.7 | 77 | −2.87 |
| 17 | c | 0.54±0.05 | 7.0±0.8 | 77 | −2.80 |
| 17 | d | 0.68±0.05 | 6.0±0.7 | 113 | −2.70 |
| 17 | e | 0.48±0.04 | 2.0±0.5 | 240 | −2.85 |
| 17 | f | 1.49±0.09 | 3.0±2.0 | 497 | −2.37 |
| 169 | a | 0.37±0.04 | 0.8±0.4 | 462 | −2.96 |
| 169 | b | 0.15±0.03 | 4.0±0.7 | 38 | −3.36 |
| 169 | c | 0.16±0.03 | 0.8±0.5 | 200 | −3.33 |
| 217 | a | 0.73±0.06 | 4.0±0.1 | 183 | −2.67 |
| 217 | b | 0.73±0.06 | 10±1 | 73 | −2.67 |
| 217 | c | 0.20±0.03 | 4.0±0.8 | 50 | −3.23 |
| 260 | a | 0.18±0.03 | 2.7±0.5 | 67 | −3.29 |
| 328 | a | 2.15±0.14 | 114±3 | 19 | −2.20 |
| 350 | a | 0.22±0.05 | 3.0±0.6 | 73 | −3.19 |
| 477 | a | 0.27±0.04 | 5.0±0.8 | 54 | −3.10 |
| 530 | a | 0.26±0.03 | 19±1 | 14 | −3.12 |
| 530 | b | 0.18±0.03 | 18±1 | 10 | −3.28 |
| 826 | a | 1.79±0.06 | 60±2 | 30 | −2.28 |
| 826 | b | 0.11±0.02 | 30±1 | 4 | −3.49 |
| 826 | c | 0.40±0.03 | 10±30 | 40 | −2.93 |
| 826 | d | 0.31±0.03 | 3.0±0.3 | 103 | −3.04 |
| 963 | a | 1.65±0.08 | 51±2 | 32 | −2.32 |
| 1455 | a | 1.65±0.09 | 90±3 | 18 | −2.31 |
| 1465 | a | 3.04±0.06 | 50±1 | 61 | −2.05 |

**Figure captions**

- Fig. 1: Distribution of LSB dwarfs studied here and HSB dwarfs from AB98 projected on the Virgo cluster. The different sub-clusterings identified by Hoffman *et al.* are indicated schematically. BCD galaxies are represented as filled circles and LSBs are empty circles. The size of the symbols is proportional to the blue magnitude of each galaxy in the VCC.

- Fig. 2: Mosaic of H$\alpha$ line (left), continuum (center), and net-H$\alpha$ (right) images of four galaxies in the LSB sample. North is up and East is to the left. The scale is indicated by a 10 arcsec long bar in the top right corner. The galaxies shown are (top to bottom) VCC 17, VCC 169, VCC 217, and VCC 260.

- Fig. 3: Same as Fig. 2. The galaxies shown are VCC 328, VCC 329, VCC 350, and VCC 367.

- Fig. 4: Same as Fig. 2. The galaxies shown are VCC 381, VCC 477, VCC 530, and VCC 565.

- Fig. 5: Same as Fig. 2. The galaxies shown are VCC 584, VCC 826, VCC 1455, and VCC 1465.

- Fig. 6: Same as Fig. 2. The galaxies shown are VCC 1585, VCC 1753, VCC 1784, and VCC 1816.

- Fig. 7: Same as Fig. 2. The galaxies shown are VCC 1822, VCC 1952, VCC 1992, and VCC 2034.

- Fig. 8: Same as Fig. 2. The galaxies shown are VCC 1822, VCC 1952, VCC 1992, and VCC 2034.

- Fig. 9: Mosaic of line (left), continuum (center), and net-H$\alpha$ (right) images of four galaxies in the HSB sample. North is up and East is to the left. The scale

Table 4—Continued

| Galaxy (VCC) | HII region ID | F(H$\alpha$) | f(OFF) | EW(H$\alpha$) | log(SFR) |
|---|---|---|---|---|---|
| 1465 | b | 0.99±0.04 | 30±1 | 33 | −2.53 |
| 1468 | a | 3.17±0.08 | 36±1 | 88 | −2.03 |
| 1585 | a | 3.94±0.14 | 76±3 | 52 | −1.93 |
| 1585 | b | 1.74±0.10 | 74±3 | 24 | −2.29 |
| 1585 | c | 0.49±0.07 | 50±3 | 10 | −2.84 |
| 1585 | d | 0.38±0.05 | 10±1 | 38 | −2.95 |
| 1753 | a | 0.32±0.06 | 10±1 | 32 | −3.02 |
| 1753 | b | 0.20±0.04 | 10±1 | 20 | −3.23 |
| 1753 | c | 0.13±0.03 | 5±1 | 26 | −3.42 |
| 1952 | a | 1.31±0.09 | 30±2 | 44 | −2.41 |
| 1952 | b | 0.80±0.08 | 70±3 | 11 | −2.63 |
| 1992 | a | 2.45±0.10 | 40±2 | 61 | −2.14 |
| 1992 | b | 2.53±0.11 | 90±3 | 28 | −2.13 |

Note. — F(H$\alpha$) is in $10^{-14}$ erg cm$^{-2}$ s$^{-1}$ and f(OFF) is in $10^{-17}$ erg cm$^{-2}$ s$^{-1}$ Å $^{-1}$. The SFR calculation is explained in the text. The equivalent width of the line is obtained by EW=$\frac{F(H\alpha)}{f(OFF)}$. The HII region labelled $f$ in VCC 17 appears on a particularly faint part of the galaxy; we could not measure the underlying continuum accurately enough to provide a good quality H$\alpha$ equivalent width.

Table 5.  Properties of individual HII regions in HSB galaxies

| Galaxy (VCC) | HII region ID | F(Hα) | f(OFF) | EW(Hα) | log(SFR) |
|---|---|---|---|---|---|
| 10 | a | 8.57±1.76 | 0.23±0.05 | 37 | −1.60 |
| 144 | a | 71.00±3.23 | 0.42±0.07 | 169 | −0.68 |
| 324 | a | 60.9±4.21 | 0.59±0.10 | 104 | −0.75 |
| 410 | a | 4.16±0.38 | 0.05±0.01 | 90 | −1.91 |
| 459 | a | 20.5±2.36 | 0.23±0.04 | 87 | −1.22 |
| 513 | a | 20.7±1.91 | 0.31±0.06 | 68 | −1.22 |
| 562 | a | 12.7±0.88 | 0.08±0.01 | 154 | −1.43 |
| 985 | a | 1.44±0.23 | 0.05±0.02 | 30 | −2.37 |
| 1179 | a | 5.77±2.26 | 0.13±0.05 | 46 | −1.77 |
| 1374 | a | 21.3±0.98 | 0.25±0.05 | 84 | −1.20 |
| 1374 | b | 3.86±0.18 | 0.18±0.08 | 22 | −1.95 |
| 1374 | c | 1.78±0.08 | 0.06±0.06 | 32 | −2.29 |
| 1725 | a | 10.13±1.17 | 0.10±0.02 | 98 | −1.53 |
| 1725 | b | 5.86±0.68 | 0.09±0.02 | 63 | −1.76 |
| 1791 | a | 7.25±0.33 | 0.05±0.01 | 135 | −1.67 |
| 1791 | b | 5.89±0.27 | 0.05±0.01 | 129 | −1.76 |
| 1791 | c | 11.1±0.51 | 0.15±0.03 | 76 | −1.49 |
| 1791 | d | 2.19±0.10 | 0.07±0.03 | 30 | −2.19 |

Note. — F(Hα) and f(OFF) are in $10^{-14}$ erg cm$^{-2}$ s$^{-1}$. The SFR calculation is explained in the text. The equivalent width of the line is obtained by EW=$\frac{F(H\alpha)}{f(OFF)}$.

is indicated by a 10 arcsec long bar in the top right corner for each object. The galaxies shown are (top to bottom) VCC 10, VCC 144, VCC 172, and VCC 324.

- Fig. 10: Same as Fig. 9. The galaxies shown are VCC 410, VCC 459, VCC 513, VCC 562, and VCC 985.

- Fig. 11: Same as Fig. 9. The galaxies shown are VCC 1179, VCC 1374, VCC 1725, and VCC 1791.

- Fig. 12: Distribution of star formation rates for individual HII regions in the HSB and LSB galaxy samples.

- Fig. 13: Correlation between the logarithms of the H$\alpha$ emission and of the red continuum light for individual HII regions in LSB galaxies. The data for HII regions of BCDs is plotted as squares and that for the HII regions of LSBs is represented by stars. The units are $10^{-14}$ erg cm$^{-2}$ s$^{-1}$ for the line flux and $10^{-14}$ erg cm$^{-2}$ s$^{-1}$ Å$^{-1}$ for the continuum flux density.

- Fig. 14: Distribution of the coverage factor of a galaxy by HII regions.

- Fig. 15: H$\alpha$ line contrast *vs.* off-line continuum contrast between the brightest and the faintest HII regions we detected in galaxies with multiple HII regions.
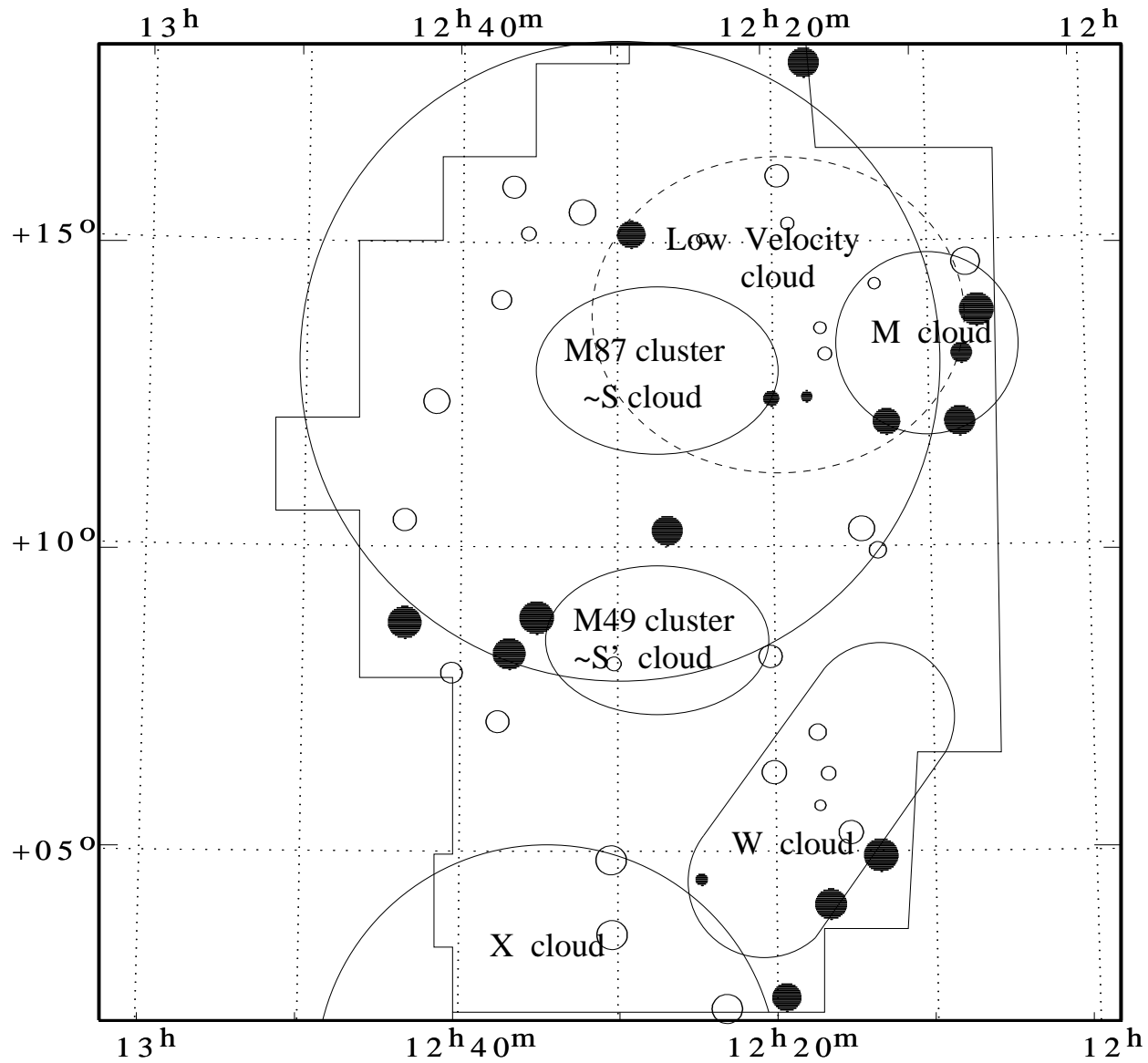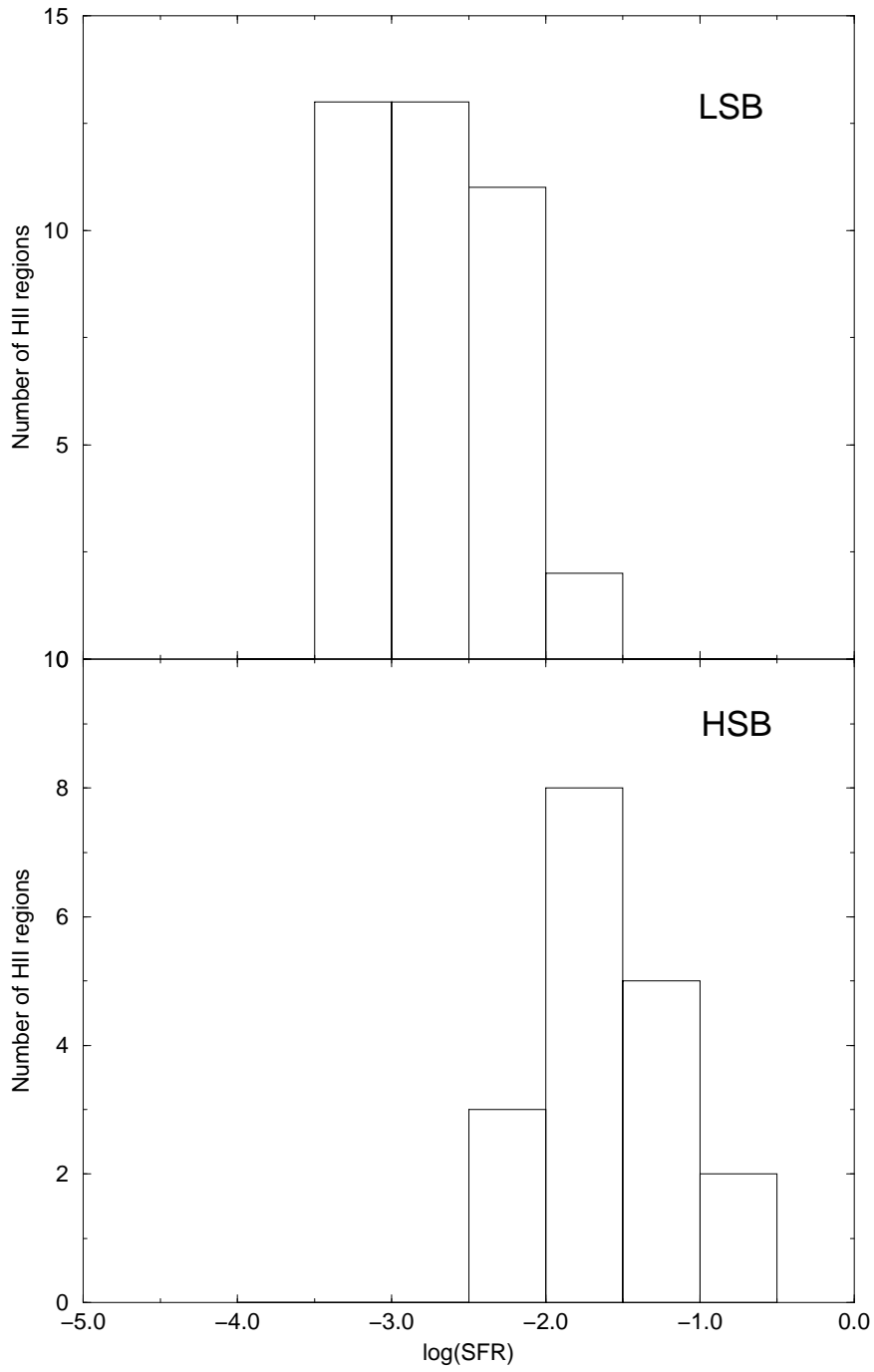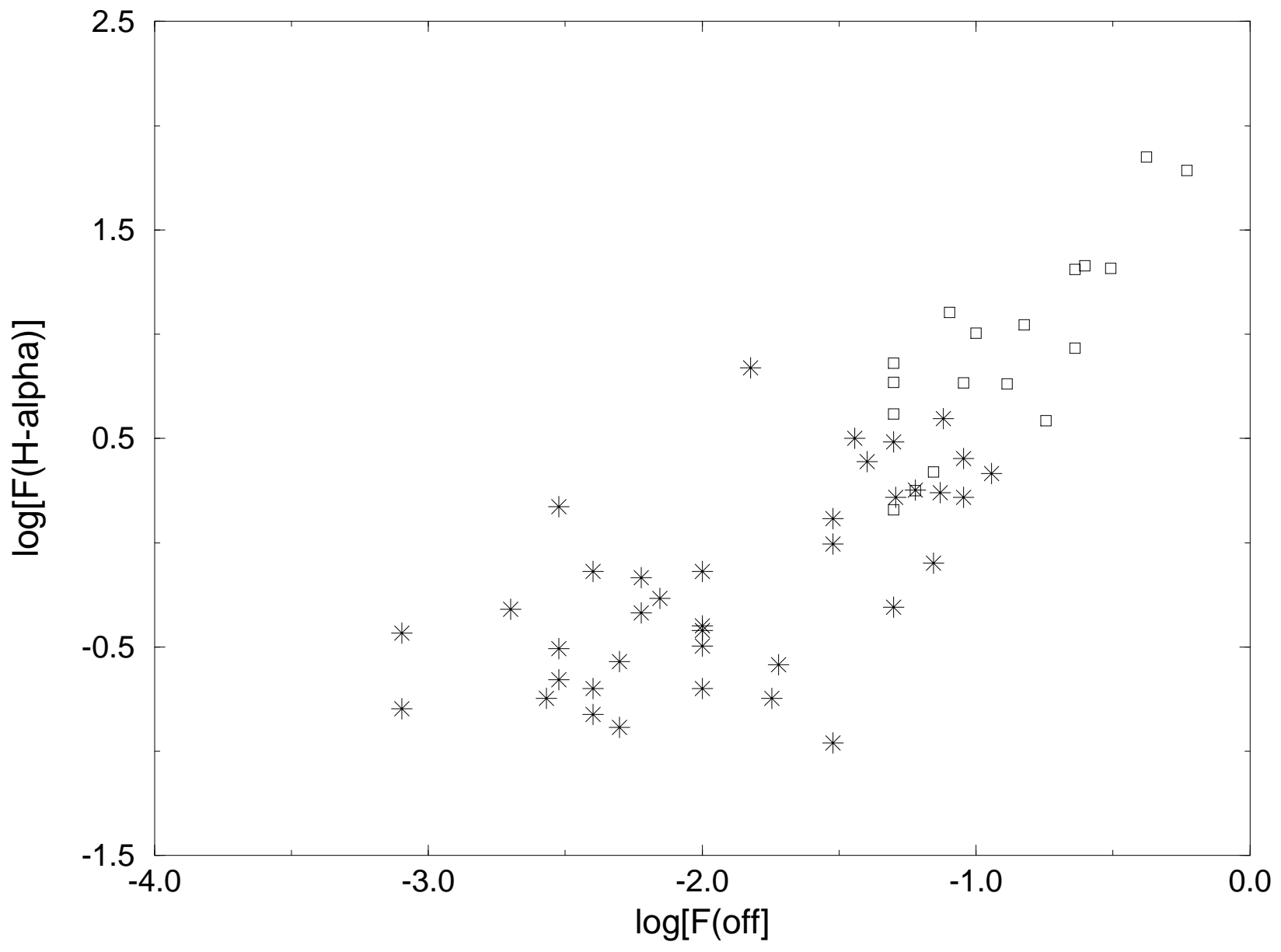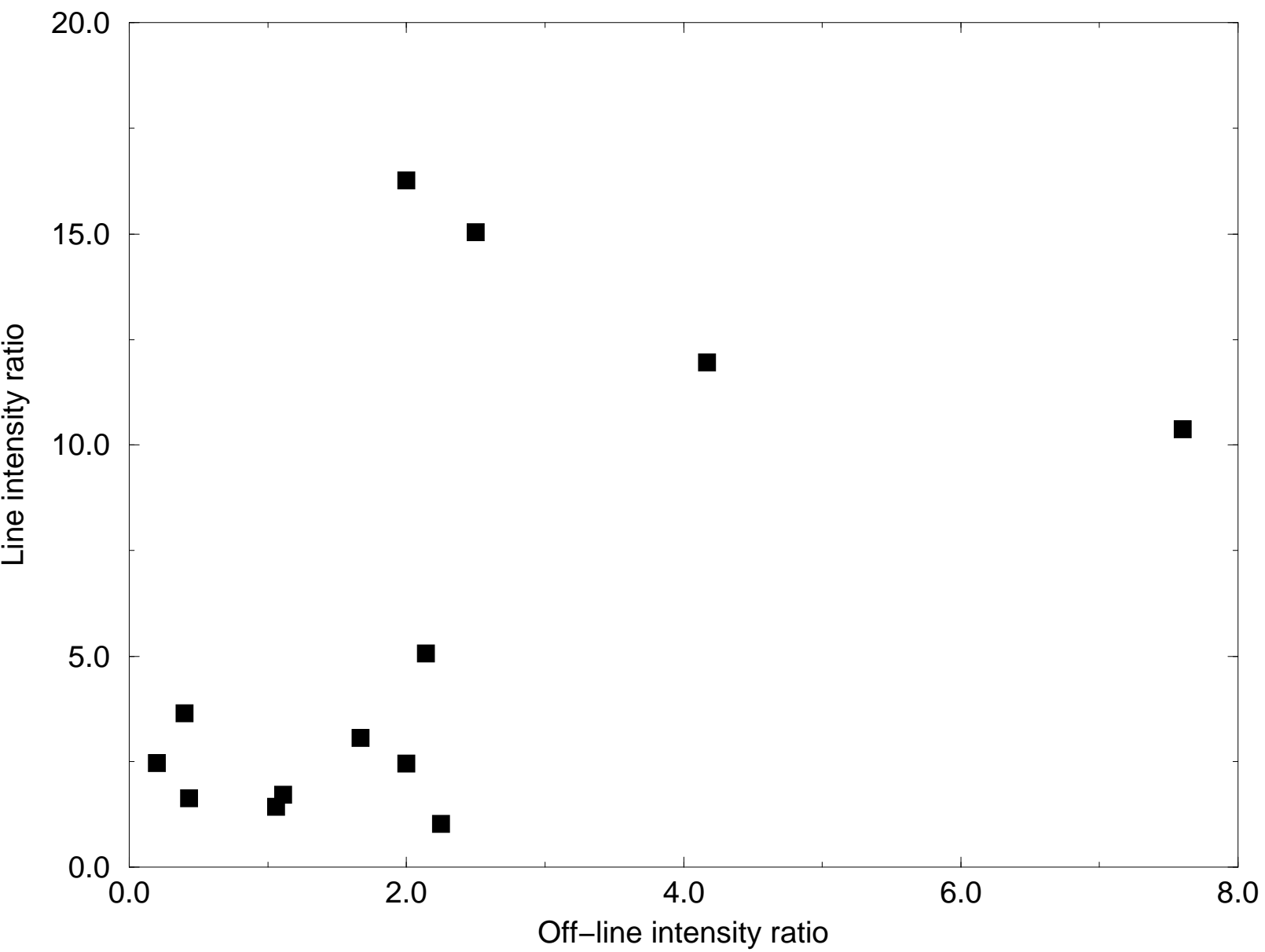
This figure "mos4x3a.a.jpg" is available in "jpg" format from:

http://il.arXiv.org/ps/astro-ph/9811427

This figure "mos4x3a.bcd.jpg" is available in "jpg" format from:

http://il.arXiv.org/ps/astro-ph/9811427

This figure "mos4x3b.a.jpg" is available in "jpg" format from:

http://il.arXiv.org/ps/astro-ph/9811427

This figure "mos4x3c.Anew.jpg" is available in "jpg" format from:

http://il.arXiv.org/ps/astro-ph/9811427

This figure "mos4x3c.bcd.jpg" is available in "jpg" format from:

http://il.arXiv.org/ps/astro-ph/9811427

This figure "mos4x3d.a.jpg" is available in "jpg" format from:

http://il.arXiv.org/ps/astro-ph/9811427

This figure "mos4x3e.a.jpg" is available in "jpg" format from:

http://il.arXiv.org/ps/astro-ph/9811427

This figure "mos4x3f.a.jpg" is available in "jpg" format from:

http://il.arXiv.org/ps/astro-ph/9811427

This figure "mos4x3z.a.jpg" is available in "jpg" format from:

http://il.arXiv.org/ps/astro-ph/9811427

This figure "mos5x3b.bcd.jpg" is available in "jpg" format from:

http://il.arXiv.org/ps/astro-ph/9811427